Magnetization-dependent inverse spin Hall effect in compensated ferrimagnet TbCo alloys

A. Yagmur ![ORCID],[*] S. Sumi, H. Awano ![ORCID], and K. Tanabe ![ORCID]

Toyota Technological Institute, Nagoya 468-8511, Japan

In this paper, we demonstrate the magnetization-dependent inverse spin Hall effect (MD-ISHE) in $Tb_xCo_{100-x}/Pt/Y_3Fe_5O_{12}$ devices using the spin Seebeck effect. It was found that a thermally injected spin current is precessed around the magnetization of the Tb_xCo_{100-x} alloy before it is converted into a charge current. Furthermore, the sign of the MD-ISHE voltage was found to depend on the Co magnetic moment direction, whereas the sign and magnitude of the conventional ISHE voltage are independent of the Tb_xCo_{100-x} magnetization direction. Meanwhile, the spin rotation angle was estimated to be ~12% in Tb_xCo_{100-x}/Pt. Our findings demonstrate that perpendicularly magnetized Tb_xCo_{100-x} supplies additional symmetry to the ISHE and provides advantages in terms of tailoring the sign of the spin-current polarization through adjusting the alloy composition.

I. INTRODUCTION

The spin Hall effect (SHE), the generation of a spin current via a charge current due to the spin-orbit coupling from extrinsic and intrinsic mechanisms, presents a major research topic related to future spintronics devices [1–3]. This spin current can be used to induce a torque effect in an adjacent magnetic material, the so-called spin-orbit torque, which could be useful for switching the magnetization direction and moving the magnetic domain walls in magnetic memory applications [4–7]. The conventional inverse SHE (ISHE), the reciprocal effect of SHE, has also been widely used to convert a spin current into a charge current, enabling the electric detection of the spin current [Fig. 1(a)] [8,9]. The early related studies mainly focused on nonmagnetic heavy metals (e.g., Pt, Ta, and W) and diluted alloys with heavy impurities (e.g., CuPt, CuBi, and AuPt) to clarify the mechanism and improve the spin-charge interconversion efficiency [10–13], whereas more recent studies have demonstrated that ferromagnetic and antiferromagnetic materials also exhibit significant SHE and ISHE [14–17].

Spin-current generation and detection have recently been observed to have gained additional symmetry in ferromagnetic and antiferromagnetic materials [15], but both Humphries *et al.* [18] and Baek *et al.* [19] demonstrated that an interface-generated spin current could result in a spin torque in an adjacent magnetic layer, depending on the adjacent material magnetization direction. The origin of this torque is attributed to the spin rotation effect, in which the spin polarization of the spin current is precessed around the magnetization [18–21]. Following these reports, both Aljuaid *et al.* [22] and Chuang *et al.* [23] demonstrated that a spin current thermally injected into a perpendicularly magnetized material experiences a precession at the interface before it

is converted into a charge current, which is known as the magnetization-dependent ISHE (MD-ISHE) [Fig. 1(b)]. To date, the spin rotation effect has been investigated only in relation to perpendicular magnetized Co/Pt or CoFeB/Ti devices [18,19,24]. However, the investigation of other materials with perpendicular magnetic anisotropy, which are derived from a different origin, is crucial to exploring this observed MD-ISHE phenomenon.

Rare earth–transition metal (RE-TM) alloys are promising magnetic materials for spintronics devices [25,26] since they exhibit strong bulk perpendicular magnetic anisotropy, making them thermally stable for high-density nonvolatile memory devices, although they also demonstrate strong spin-orbit coupling. In addition, RE-TM alloys are ferrimagnetic, where RE moments and TM moments couple antiferromagnetically, resulting in a low magnetization, which is favorable for various applications owing to the weak stray fields. The RE-TM alloys also exhibit a longer spin dephasing length than ferromagnetic materials [27,28], whereas the adjustable composition of these alloys allows for tailoring the magnitude and direction of the antiferromagnetically coupled magnetic moments. All these features offer the strong possibility of realizing and clarifying the MD-ISHE.

In this paper, we investigate the MD-ISHE in $Tb_xCo_{100-x}/Pt/Y_3Fe_5O_{12}$ (YIG) devices. Here, RE-TM Tb_xCo_{100-x} alloys were selected since, as noted above, they exhibit strong spin-orbit coupling and perpendicular magnetic anisotropy. In addition, the Tb_xCo_{100-x} alloy is a ferrimagnetic metal where the magnetic moments of Tb and Co couple antiferromagnetically, which means further advantages can be gained through studying the effect of the different magnetic moments. Here, we adopt the ferrimagnetic insulator YIG as a spin injector using the spin Seebeck effect (SSE), a thermal means of generating a spin current from an applied temperature gradient [29,30]. Meanwhile, the platinum (Pt) nonmagnetic conductor suppresses the coupling between the YIG and Tb_xCo_{100-x} layers.
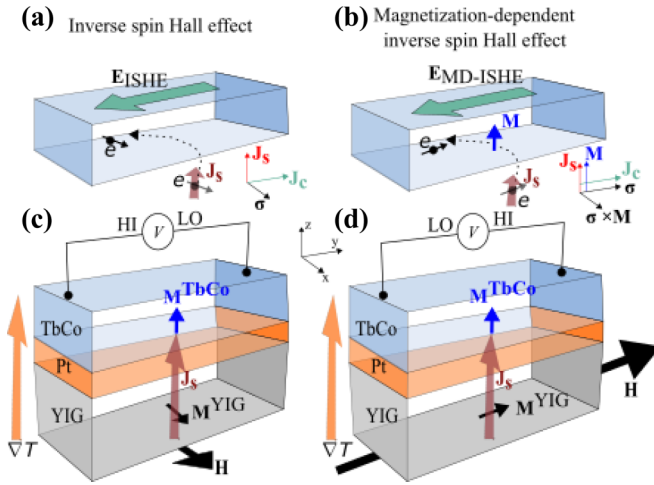
_____
*ayagmur@toyota-ti.ac.jp

FIG. 1. (a) Schematic of the inverse spin Hall effect (ISHE), where an injected spin-current $\mathbf{J}_s$ is converted into a charge-current $\mathbf{J}_c$ depending on the cross product of $\mathbf{J}_s$ and spin-polarization σ. (b) Schematic of the magnetization-dependent ISHE (MD-ISHE), where an injected $\mathbf{J}_s$ is converted into a $\mathbf{J}_c$ depending on the cross product of $\mathbf{J}_s$, σ, and magnetization $\mathbf{M}$. Schematics of the measurement condition for (c) the ISHE, where the applied magnetic field $\mathbf{H}$ was applied along the x direction (orthogonal to the electrodes) and (d) the MD-ISHE, where the $\mathbf{H}$ was applied along the y direction (parallel to the electrodes) for the TbCo/Pt/YIG samples. Here, $\mathbf{M}^{\mathrm{TbCo}}$, $\mathbf{M}^{\mathrm{YIG}}$, ∇T, and V represent the magnetization of the TbCo alloy and YIG, the applied temperature gradient, and the induced voltage signal, respectively.

II. EXPERIMENTAL METHODS

A schematic of our $\mathrm{Tb}_x\mathrm{Co}_{100-x}(19 \, \mathrm{nm})/\mathrm{Pt}(1 \, \mathrm{nm})/\mathrm{YIG}$ samples is shown in Figs. 1(c) and 1(d). A polycrystalline YIG with a thickness of 172 ± 9 nm (measured via ellipsometry) was grown on a $\mathrm{SiO}_2/\mathrm{Si}$ substrate with a thickness of 0.4 mm using a sputtering system at room temperature before it was annealed at $800\,^{\circ}\mathrm{C}$ for 2 h in air to obtain a polycrystalline YIG. The $\mathrm{YIG}/\mathrm{SiO}_2/\mathrm{Si}$ was then precisely cut into $2(\pm 0.1) \times 10(\pm 0.1)\,\mathrm{mm}^2$ rectangular shapes from the same substrate using a precision crystal cutter before the Pt layer was sputtered onto the YIG. After this, the $\mathrm{Tb}_x\mathrm{Co}_{100-x}$ alloy layer was deposited via the cosputtering method from the Co and Tb targets, meaning the composition of the alloy could be changed by adjusting the cosputtering power while the Tb sputtering power remained fixed. A 19-nm-thick $\mathrm{Tb}_x\mathrm{Co}_{100-x}$ was selected to obtain a magnetization compensation composition of around $x = 21$ since the $\mathrm{Tb}_x\mathrm{Co}_{100-x}$ layer thickness is an important factor, having the capacity of changing the magnetic compensation because of the formation of boundary layers at the interfaces [31]. However, it should be noted that a comparatively thinner $\mathrm{Tb}_x\mathrm{Co}_{100-x}$ layer may also exhibits perpendicular magnetic anisotropy and would thus be suitable for the investigation of the MD-ISHE. The labeled thicknesses of the Pt and $\mathrm{Tb}_x\mathrm{Co}_{100-x}$ layers represent the estimated results using the sputtering rates. A 10-nm SiN layer was fabricated on top of the $\mathrm{Tb}_x\mathrm{Co}_{100-x}$ layer to prevent oxidization. The sputtering process was carried out at room temperature, with the Co and Tb mixed naturally without any annealing process. The substrates were rotated during

the sputtering process to ensure the formation of a uniform thickness, and various $\mathrm{Tb}_x\mathrm{Co}_{100-x}(19 \, \mathrm{nm})/\mathrm{Pt}(1 \, \mathrm{nm})/\mathrm{SiO}_2/\mathrm{Si}$ samples were fabricated at the same time. Here, the $\mathrm{Tb}_x\mathrm{Co}_{100-x}(19 \, \mathrm{nm})/\mathrm{Pt}(1 \, \mathrm{nm})/\mathrm{SiO}_2/\mathrm{Si}$ samples were used to assess the sample compositions via energy-dispersive x-ray spectrometry since it was important to avoid contamination from the YIG layer. The measured compositions were consistent with the expected compositions. The crystalline structure of the $\mathrm{Tb}_x\mathrm{Co}_{100-x}$ layer was amorphous because of the different sizes of the Co and Tb atoms and the high-energy deposition technique. The magnetic properties of the $\mathrm{Tb}_x\mathrm{Co}_{100-x}(19 \, \mathrm{nm})/\mathrm{Pt}(1 \, \mathrm{nm})/\mathrm{YIG}/\mathrm{SiO}_2/\mathrm{Si}$ were measured using a vibrating sample magnetometer (VSM) and the polar magneto-optical Kerr effect (PMOKE).

To detect the ISHE and MD-ISHE in the $\mathrm{Tb}_x\mathrm{Co}_{100-x}$ (19 nm)/Pt(1 nm)/YIG samples, SSE voltage measurements were performed in a longitudinal configuration [32]. When a temperature gradient (∇T) was applied to the $\mathrm{Tb}_x\mathrm{Co}_{100-x}/\mathrm{Pt}/\mathrm{YIG}$ sample, a spin current ($\mathbf{J}_s$) with the spin-polarization σ set by the magnetization of the YIG was thermally injected from the YIG into the Pt and $\mathrm{Tb}_x\mathrm{Co}_{100-x}$ layers along the ∇T direction. This spin current was converted into a charge current ($\mathbf{J}_c$) due to the ISHE and MD-ISHE [8,9,22,23]. When the magnetization of the YIG is along the x direction, a $\mathbf{J}_c$ can be expected to be generated along the y direction [Fig. 1(c)] as follows:

$$\mathbf{J}_c = (2e/\hbar)\theta_{\mathrm{SH}}\mathbf{J}_s \times \sigma, \tag{1}$$

where e, $\hbar$, and θ_{SH} are the elementary charge, Planck constant, and spin Hall angle of $\mathrm{Tb}_x\mathrm{Co}_{100-x}/\mathrm{Pt}$, respectively.

Meanwhile, when the magnetization of the YIG ($\mathbf{M}^{\mathrm{YIG}}$) and the magnetization of the TbCo alloy ($\mathbf{M}^{\mathrm{TbCo}}$) are along the y and z directions, respectively, a $\mathbf{J}_c$ can be expected to be generated along the y direction [Fig. 1(d)] as follows [18,23]:

$$\mathbf{J}_c = (2e/\hbar)\theta_{\mathrm{MD-SH}}\mathbf{J}_s \times (\sigma \times \mathbf{n}^{\mathrm{TbCo}}), \tag{2}$$

where $\theta_{\mathrm{MD-SH}}$ is the magnetization-dependent spin Hall angle of $\mathrm{Tb}_x\mathrm{Co}_{100-x}/\mathrm{Pt}$, and $\mathbf{n}^{\mathrm{TbCo}}$ is the normalized magnetization of the TbCo alloy ($\mathbf{M}^{\mathrm{TbCo}}/|\mathbf{M}^{\mathrm{TbCo}}|$). It should be noted that the polarity of the MD-ISHE signal was associated with the magnetizations of the YIG and $\mathrm{Tb}_x\mathrm{Co}_{100-x}$ layers. Two main mechanisms can explain the spin rotation effect [18,21,22,33,34], with one possible physical mechanism for the MD-ISHE, the interface-spin precession effect [20,22,34]. Here, when
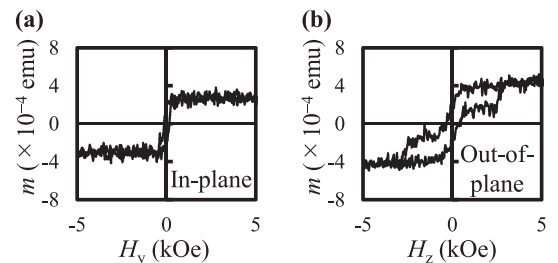

FIG. 2. Vibrating sample magnetometry hysteresis loops measured for the $\mathrm{Tb}_{14}\mathrm{Co}_{86}/\mathrm{Pt}/\mathrm{YIG}$ sample in (a) the in-plane direction and (b) the out-of-plane direction.
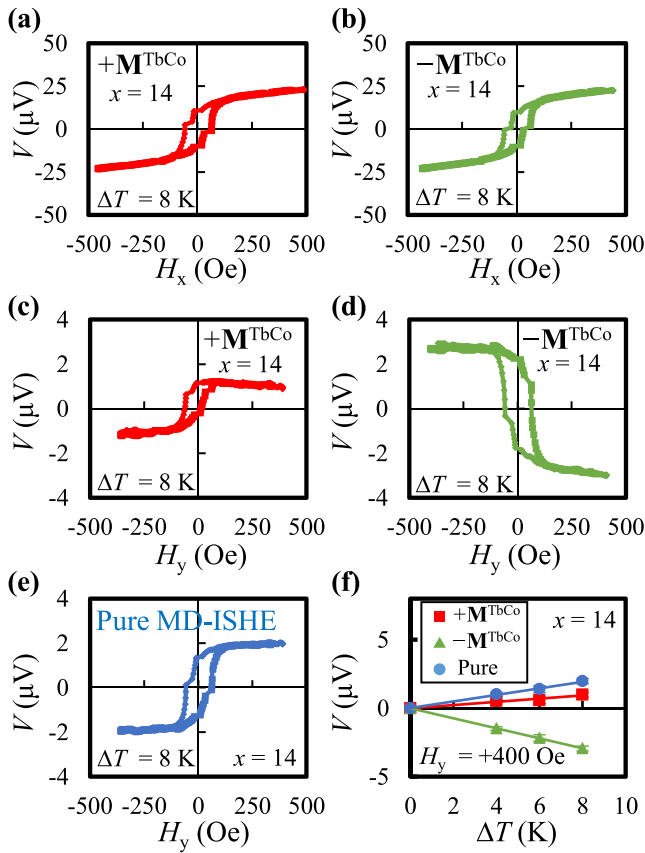
FIG. 3. V as a function of H_x at $\Delta T = 8\,\mathrm{K}$ for the Tb$_{14}$Co$_{86}$/Pt/YIG sample, where the TbCo magnetization was aligned along (a) the $+z$ direction ($+\mathbf{M}^{\mathrm{TbCo}}$) and (b) the $-z$ direction ($-\mathbf{M}^{\mathrm{TbCo}}$). V as a function of H_y at $\Delta T = 8\,\mathrm{K}$ for the Tb$_{14}$Co$_{86}$/Pt/YIG sample where the TbCo magnetization was aligned along (c) the $+z$ direction ($+\mathbf{M}^{\mathrm{TbCo}}$) and (d) the $-z$ direction ($-\mathbf{M}^{\mathrm{TbCo}}$). (e) Pure magnetization-dependent inverse spin Hall effect (MD-ISHE) V as a function of H_y at $\Delta T = 8\,\mathrm{K}$ for the Tb$_{14}$Co$_{86}$/Pt/YIG sample, where the TbCo magnetization was aligned along the $+z$ direction, obtained by subtracting the (d) data from those in (c) and dividing the result by two. (f) ΔT dependence of the V signal in the $+\mathbf{M}^{\mathrm{TbCo}}$, $-\mathbf{M}^{\mathrm{TbCo}}$, and pure MD-ISHE conditions at $H_y = +400\,\mathrm{Oe}$ for the Tb$_{14}$Co$_{86}$/Pt/YIG sample.

the spin current is injected into the Tb$_x$Co$_{100-x}$/Pt, the spin polarization experiences a rotation around the magnetization owing to the interface spin-orbit coupling at the interface. Meanwhile, the second possible mechanism is the spin swapping effect resulting from the bulk spin-orbit coupling of Tb$_x$Co$_{100-x}$, which has a similar origin of skew scattering [22,35–38]. The polarized electrons are scattered by the impurities, and the directions of the spin-current flow and spin polarization are interchanged.

The experimental setup used in this paper was like that used in conventional SSE [32,39]. The samples were sandwiched between two AlN heat baths in which the temperatures were stabilized to $300\,\mathrm{K} + \Delta T$ and $300\,\mathrm{K}$ to apply ∇T along the z direction. A ceramic heater was used to generate the temperature difference ΔT, which was measured using two thermocouples. Initially, the $\mathbf{M}^{\mathrm{TbCo}}$ was saturated along the
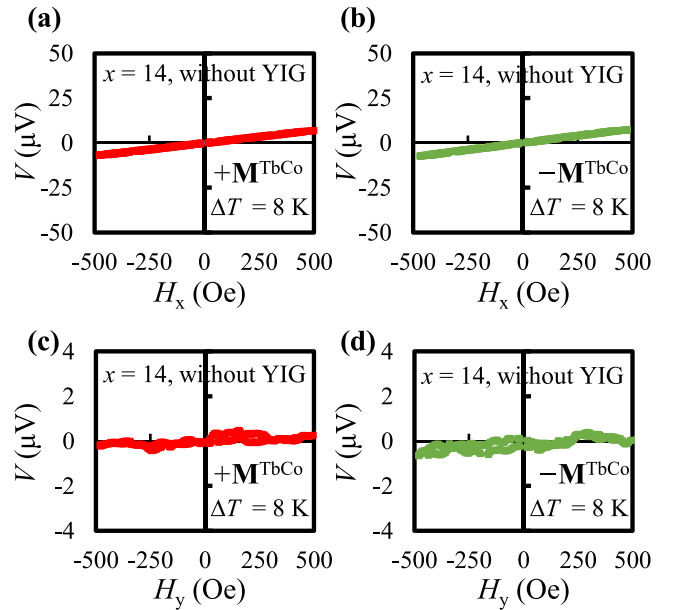

FIG. 4. V as a function of H_x at $\Delta T = 8\,\mathrm{K}$ for the Tb$_{14}$Co$_{86}$/Pt/SiO$_2$/Si sample where the TbCo magnetization was aligned along (a) the $+z$ direction ($+\mathbf{M}^{\mathrm{TbCo}}$) and (b) the $-z$ direction ($-\mathbf{M}^{\mathrm{TbCo}}$). V as a function of H_x at $\Delta T = 8\,\mathrm{K}$ for the Tb$_{14}$Co$_{86}$/Pt/SiO$_2$/Si sample where the TbCo magnetization was aligned along (c) the $+z$ direction ($+\mathbf{M}^{\mathrm{TbCo}}$) and (d) the $-z$ direction ($-\mathbf{M}^{\mathrm{TbCo}}$).

z direction by applying $\mathbf{H}_z$. Then by applying ∇T and an external magnetic field $\mathbf{H}_x$ with the magnitude H_x ($\mathbf{H}_y$ with the magnitude H_y) to the samples, we measured the voltage V signals due to the ISHE (MD-ISHE) between the ends of the samples. Here, $\mathbf{H}_x$ and $\mathbf{H}_y$ were applied to tailor the magnetization of the YIG layer, in which the spin polarization of the thermally induced spin current was determined [Figs. 1(c) and 1(d)]. Since the TbCo alloys exhibit strong perpendicular magnetic anisotropy, their magnetizations remained at the z direction, whereas the in-plane magnetic fields were swept between $+500$ and $-500\,\mathrm{Oe}$.

III. RESULTS AND DISCUSSION

Figure 2(a) shows the VSM hysteresis loops measured for the Tb$_{14}$Co$_{86}$/Pt/YIG sample in the in-plane direction. Here, the sharp switching at a low field ($\sim$70 Oe) corresponded to the YIG magnetization. Meanwhile, Fig. 2(b) shows the VSM hysteresis loops measured for the Tb$_{14}$Co$_{86}$/Pt/YIG sample in the out-of-plane direction. Here, the YIG magnetization required a larger field for the switching (1000 Oe). Importantly, the Tb$_{14}$Co$_{86}$ magnetization had a sharp switch at a larger field (2500 Oe), revealing the perpendicular magnetic anisotropy. It was determined that the YIG exhibited in-plane magnetic anisotropy with a saturation magnetization of $\sim$87 emu/cm^3 [40]. Similar results were obtained for all the Tb$_x$Co$_{100-x}$(19 nm)/Pt(1 nm)/YIG samples. It should be noted that 1-nm Pt may be formed in terms of an islandlike arrangement on the YIG surface. Moreover, it is believed that strong anisotropic pair-pair correlations may sustain the perpendicular magnetic
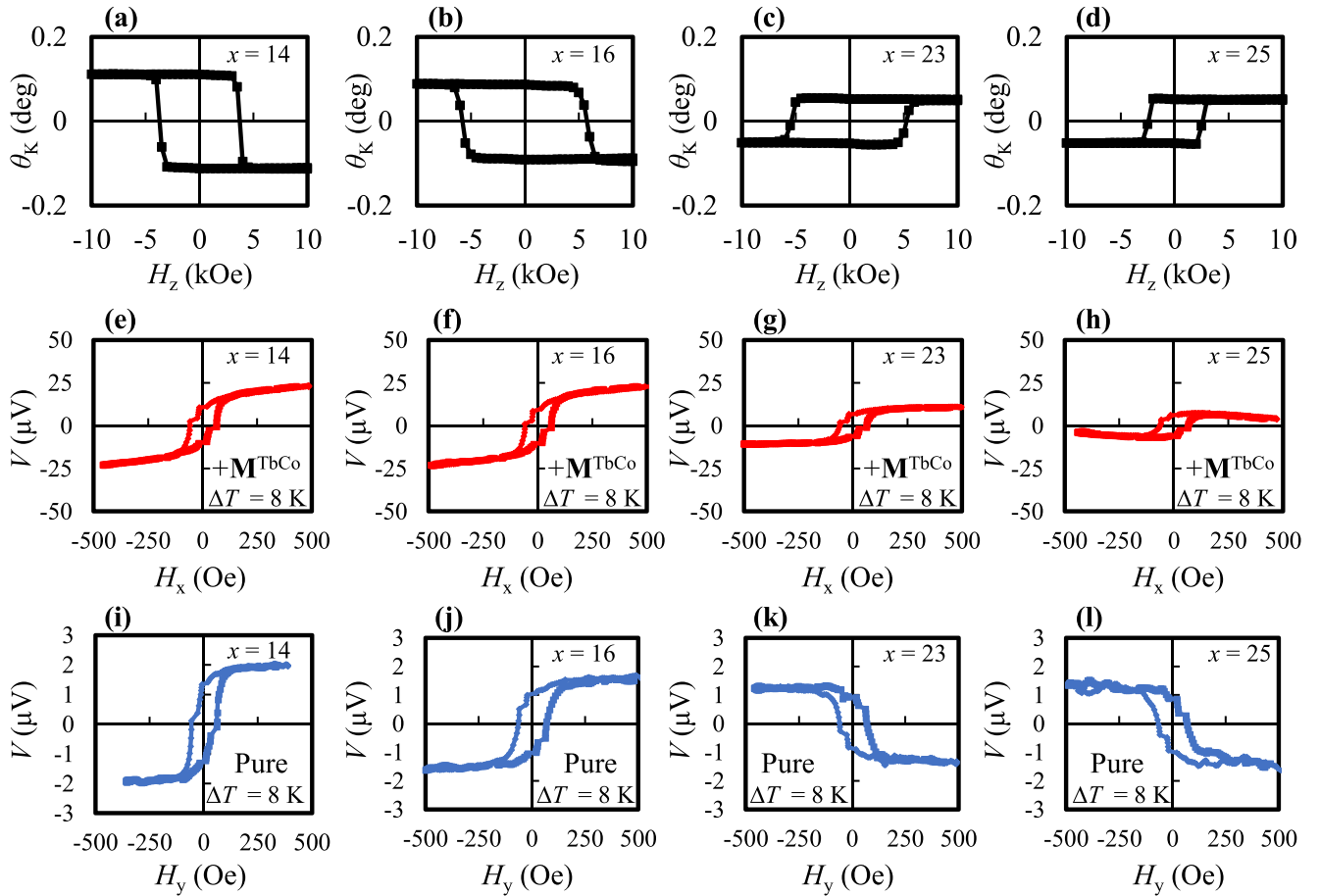
FIG. 5. (a)–(d) Polar magneto-optical Kerr effect (PMOKE) loops for the Tb_xCo_{100-x}(19 nm)/Pt(1 nm)/YIG samples, where $x = 14$, 16, 23, and 25, respectively. (e)–(h) The V in the Tb_xCo_{100-x}/Pt/YIG samples, where $x = 14$, 16, 23, and 25, respectively, as a function of H_x at $\Delta T = 8$ K with the TbCo magnetization saturated along the $+z$ direction ($+\mathbf{M}^{TbCo}$). (i)–(l) The V in the Tb_xCo_{100-x}/Pt/YIG samples, where $x = 14$, 16, 23, and 25, respectively, as a function of H_y at $\Delta T = 8$ K, where the $-\mathbf{M}^{TbCo}$ data were subtracted from the $+\mathbf{M}^{TbCo}$ data and the result divided by two.

anisotropy in the entire volume of TbCo [41,42]. Meanwhile, a Pt(1 nm)/YIG sample was fabricated, and it was confirmed that only 1-nm Pt was conductive on the YIG layer. The measured resistivity was 4.1×10^{-6} Ω m, which is a typical value for an ultrathin Pt layer on YIG [43]. Therefore, based on the VSM and PMOKE results, it was concluded that the Tb_xCo_{100-x}(19 nm)/Pt(1 nm)/YIG samples exhibited relatively weak interlayer exchange coupling and that YIG and TbCo alloy magnetizations were decoupled.

Figure 3(a) shows the V in the $Tb_{14}Co_{86}$/Pt/YIG sample as a function of H_x at $\Delta T = 8$ K, where the $Tb_{14}Co_{86}$ alloy magnetization was initially aligned along the $+z$ direction ($+\mathbf{M}^{TbCo}$). Here, it was found that a clear V signal appeared in the $Tb_{14}Co_{86}$/Pt/YIG sample, in which the polarity was determined according to the magnetization of the YIG layer. To clarify the magnetization dependence, the $Tb_{14}Co_{86}$/Pt/YIG sample was also measured, where the $\mathbf{M}^{TbCo}$ was initially aligned along the $-z$ direction ($-\mathbf{M}^{TbCo}$) [Fig. 3(b)]. The magnitude and sign of the V signals were similar in both the $+\mathbf{M}^{TbCo}$ and $-\mathbf{M}^{TbCo}$ conditions. This behavior was in good agreement with the features of the SSE and ISHE [44]. Meanwhile, it should be noted that the sign of θ_{SH} is the same

as that of Pt and Co [44]. Figures 3(c) and 3(d) show the V in the $Tb_{14}Co_{86}$/Pt/YIG sample as a function of H_y at $\Delta T = 8$ K, where the TbCo alloy magnetization was initially aligned along the $+z$ and $-z$ directions ($+\mathbf{M}^{TbCo}$ and $-\mathbf{M}^{TbCo}$), respectively. Here, V signals were observed in which, based on Eq. (1), we expected no ISHE contribution. In addition, the V signals exhibited a different polarity depending on the direction of the $\mathbf{M}^{TbCo}$, which was both consistent with Eq. (2) and clear evidence for the MD-ISHE [22,23]. Here, it should be noted that the direction of the applied $\mathbf{H}_y$ was the same for both the $+\mathbf{M}^{TbCo}$ and $-\mathbf{M}^{TbCo}$ conditions. However, the different values for the amplitude of V signals may have been due to the initial small misalignment between the $\mathbf{H}_y$ and the voltage detection direction, which may have contributed to an unintentional ISHE voltage. The same ISHE contribution was expected for the $+\mathbf{M}^{TbCo}$ and $-\mathbf{M}^{TbCo}$ conditions, as shown in Figs. 3(c) and 3(d), since it is known that the ISHE is even (as opposed to odd) under time reversal [also shown in Figs. 3(a) and 3(b)]. To overcome this even ISHE contribution, we subtracted the $-\mathbf{M}^{TbCo}$ data from the $+\mathbf{M}^{TbCo}$ data and divided the result by two, which revealed the pure MD-ISHE V signal for the $+\mathbf{M}^{TbCo}$ condition [Fig. 3(e)]. The polarity

dependence on the $\mathbf{M}^{TbCo}$ confirmed that the MD-ISHE was odd under time reversal, which was consistent with previous reports [15,22,23]. The magnitudes of the V signals for the $+\mathbf{M}^{TbCo}$, $-\mathbf{M}^{TbCo}$, and pure MD-ISHE conditions were proportional to ΔT at $H_y = +400$ Oe [Fig. 3(f)], which was in good agreement with the features of the SSE, ISHE, and MD-ISHE [Eq. (2)]. It should also be noted that the sign of θ_{MD-SH} is the same as that of Pt/Co/Pt [23]. In addition, the V in the Tb$_{14}$Co$_{86}$/Pt/SiO$_2$/Si sample (without YIG) was measured as a function of H_x and H_y at $\Delta T = 8$ K for both the $+\mathbf{M}^{TbCo}$ and $-\mathbf{M}^{TbCo}$ conditions [Figs. 4(a)–4(d)]. Here, it was found that the ISHE and MD-ISHE V signals disappeared in the absence of the YIG layer, confirming that the spin-current injection played a critical role in the observed signals. In fact, a linearly dependent V signal was observed on the H_x, which may have been induced by the anomalous Nernst effect (ANE) due to the slightly tilted TbCo magnetization along the $\mathbf{H}_x$ direction [Figs. 4(a) and 4(b)] [44].

To further clarify the MD-ISHE in the perpendicularly magnetized TbCo alloys, various samples with different Co and Tb compositions were also fabricated. Figures 5(a)–5(d) show the PMOKE results for the Tb$_x$Co$_{100-x}$(19 nm)/Pt(1 nm)/YIG samples, where $x = 14$, 16, 23, and 25, respectively, with the results indicating that all the TbCo alloys exhibited strong perpendicular magnetic anisotropy. Importantly, the Kerr rotation angle (θ_K) signals observed for the $x = 14$ and 16 samples were opposite in sign to those observed for the $x = 23$ and 25 samples, which indicated that the magnetization of the former was dominated by the moment of Co (Co-rich TbCo alloy), whereas the magnetization of the latter was dominated by the moment of Tb (Tb-rich TbCo alloy). This was consistent with the nature of ferrimagnetic TbCo alloys [25,44]. The same SSE voltage measurements were then performed to investigate the ISHE and MD-ISHE using the Tb$_x$Co$_{100-x}$(19 nm)/Pt(1 nm)/YIG samples where $x = 14$, 16, 23, and 25. Figures 5(e)–5(h) show the V resulting from the ISHE and ANE (due to the slightly tilted TbCo magnetization along the $\mathbf{H}_x$ direction) in the Tb$_x$Co$_{100-x}$/Pt/YIG samples where $x = 14$, 16, 23, and 25, respectively, as a function of H_x at $\Delta T = 8$ K and the $+\mathbf{M}^{TbCo}$ condition. Importantly, the polarity of the observed ISHE voltage signals remained the same, whereas the linearly dependent V signals due to the ANE on the H_x were positive (negative) for the samples in which the magnetization was dominated by Co (Tb) moments. These results were consistent with those obtained in a previous report on Tb$_x$Co$_{100-x}$/Cu/YIG devices [44]. Furthermore, after aligning the TbCo magnetization along the $-z$ direction ($-\mathbf{M}^{TbCo}$), the same results were obtained, which were in good agreement with the features of the SSE, ISHE, and ANE. Figures 5(i)–5(l) show the V due to the pure MD-ISHE in the Tb$_x$Co$_{100-x}$/Pt/YIG samples where $x = 14$, 16, 23, and 25, respectively, as a function of H_y at $\Delta T = 8$ K, where the $-\mathbf{M}^{TbCo}$ data were subtracted from the $+\mathbf{M}^{TbCo}$ data and the result then divided by two. Importantly, the sign of the MD-ISHE voltage signals for the $x = 14$ and 16 samples (the Co moments dominated the magnetization) was opposite to those of the $x = 23$ and 25 samples (the Tb moments dominated the magnetization), which indicated that, unlike with the ISHE, the sublattice magnetizations played a significant role in the spin-to-charge conversion for the
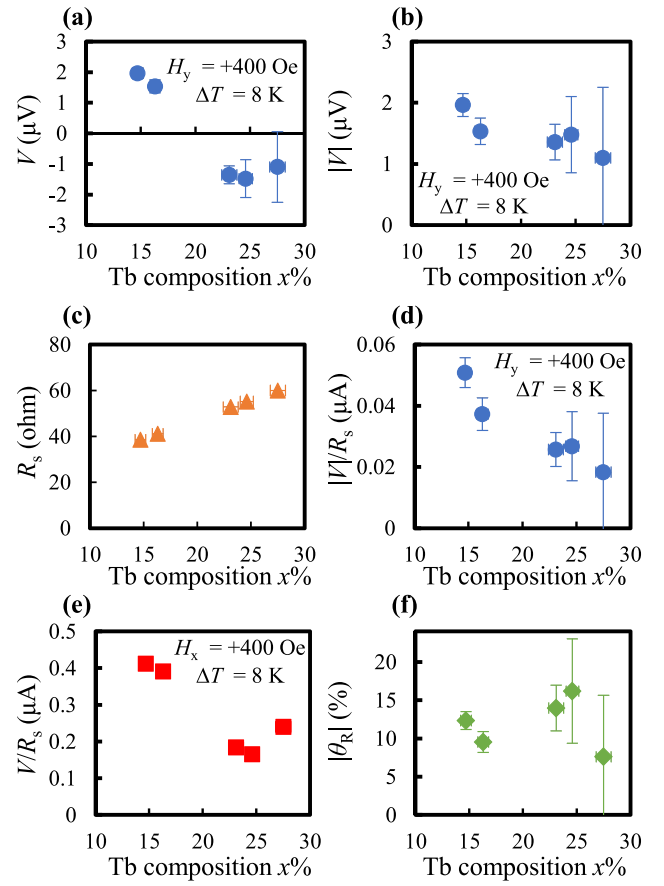
FIG. 6. (a) V and (b) $|V|$ as a function of Tb composition $x\%$ in the Tb$_x$Co$_{100-x}$/Pt/YIG samples at $H_y = +400$ Oe and $\Delta T = 8$ K. (c) The sheet resistance (R_s) of the Tb$_x$Co$_{100-x}$ alloys as a function of Tb concentration $x\%$. (d) $|V|/R_s$ as a function of Tb composition $x\%$ in the Tb$_x$Co$_{100-x}$/Pt/YIG samples at $H_y = +400$ Oe and $\Delta T = 8$ K. (e) $|V|/R_s$ as a function of Tb composition $x\%$ in the Tb$_x$Co$_{100-x}$/Pt/YIG samples at $H_x = +400$ Oe and $\Delta T = 8$ K. (f) $|\theta_R|(= |\theta_{MD-SH}/\theta_{SH}| \times 100$) as a function of Tb composition $x\%$ in the Tb$_x$Co$_{100-x}$/Pt/YIG samples.

MD-ISHE. This significant role on the Co magnetization was addressed since the $3d$ bands of the Co were close to the Fermi level, whereas the $4f$ bands of the Tb were far below it [28,45]. This indicated that the spin precession emerged more strongly with the Co moments. These observations mean that it can be concluded that the sign of the ISHE voltage is independent of the direction and concentration of the Tb and Co moments and that the sign of the MD-ISHE voltage signal can be attributed to the direction of the Co moment like the ANE.

Figure 6(a) plots the Tb composition $x\%$ dependence of the V due to the MD-ISHE (obtained by subtracting the $-\mathbf{M}^{TbCo}$ data from the $+\mathbf{M}^{TbCo}$ data and dividing the result by two) at $H_y = +400$ Oe and $\Delta T = 8$ K in the Tb$_x$Co$_{100-x}$/Pt/YIG samples. Since Tb$_x$Co$_{100-x}$ alloys are ferrimagnets, the V signals change sign around the magnetization compensation composition ($\sim 21\%$ Tb) due to the reversal of the sublattice magnetization. Meanwhile, Fig. 6(b) shows the Tb composition $x\%$ dependence of $|V|$ due to the MD-ISHE. Here, the amplitude of the V signal gradually decreased with the increase in Tb ratio, whereas the sheet resistance $R_s (= Rw/l)$

of the Tb_xCo_{100-x}/Pt increased with the increase in Tb ratio, where R, w, and l are the resistance, width, and length of the sample, respectively [Fig. 6(c)]. Figures 6(d) and 6(e) show the Tb composition x% dependence of the $|V|/R_s$ at $H_y = +400$ Oe due to the MD-ISHE and the V/R_s at $H_x = +400$ Oe due to the ISHE (after subtracting the ANE contribution) in the Tb_xCo_{100-x}/Pt/YIG samples, respectively. Both the MD-ISHE- and ISHE-induced charge-current values gradually decreased with the increase in Tb ratio. The decreasing tendency of the MD-ISHE was like that of the ISHE, indicating that the spin-to-charge conversion phenomena had a similar origin. The difference in $V/R_s(|V|/R_s)$ values was revealed via the different (magnetization dependent) spin Hall angle values of the TbCo alloys [Eqs. (1) and (2)]. Importantly, given the similar experimental conditions, the same spin injection efficiency was expected under both ISHE and MD-ISHE conditions. Based on this assumption, we could estimate the spin rotation angle according to $|\theta_R| = |\theta_{MD-SH}/\theta_{SH}| \times 100$. Here, it was found that the MD-ISHE was $12 \pm 3\%$ of the ISHE, indicating that $12 \pm 3\%$ of spin rotated around the magnetization of the Tb_xCo_{100-x} in the Tb_xCo_{100-x}/Pt/YIG sample [Fig. 6(f)], which was three times larger than that in Pt/Co/Pt/YIG [23]. Furthermore, the anomalous Hall effect (AHE) due to the ISHE-induced charge current must be considered. This contribution shares the same symmetry as the MD-ISHE but is expected to be small since the AHE angle was determined to be $1.3 \pm 0.2\%$ for our devices [46].

Finally, the remaining tasks for estimating the real spin rotation angle and for understanding the physical mechanism of the MD-ISHE must be addressed. Here, we consider the Tb_xCo_{100-x}/Pt for simplicity. As discussed above, the MD-ISHE originates from the Tb_xCo_{100-x}/Pt interface and bulk Tb_xCo_{100-x}. However, 1-nm Pt contributes to the conventional ISHE (the θ_{SH} signs of Pt and TbCo alloys are the same), and it is necessary to remove this contribution to estimate the real spin rotation angle (resulting in a larger θ_R) due to

the intrinsic TbCo alloy with the aid of other experiments and calculations. Furthermore, previous reports focused on the spin rotation effect mainly in terms of the interface effect [18,19,22,23,47], and although our results were consistent with the interface-spin precession effect, the bulk contribution should be considered in future work. The thickness dependence of TbCo alloy is a good candidate for distinguishing the interface and bulk contributions. Since TbCo alloys exhibit strong bulk perpendicular magnetic anisotropy, we can carry out a thickness-dependent study over a much larger thickness. This is not possible for the Pt/Co bilayer structure since increasing the thickness of the Co layer may result in the loss of perpendicular magnetic anisotropy.

IV. CONCLUSIONS

In conclusion, in this paper, we demonstrated the ISHE and MD-ISHE using the SSE in various Tb_xCo_{100-x}/Pt/YIG devices. It was confirmed that the polarity of the ISHE voltages in the Tb_xCo_{100-x}/Pt/YIG devices can be identified through the magnetization of the YIG and is insensitive to the magnetization of the TbCo alloy. Meanwhile, the polarity of the MD-ISHE voltage signal depends not only on the YIG magnetization but also on the direction of the Tb and Co moments. In changing the Tb concentration in the TbCo alloys, the spin-to-charge conversion efficiency was altered; however, the spin rotation efficiency was ~12%. Our results demonstrate that RE-TM alloys could be useful for the MD-ISHE and could provide further strategies for spintronics devices.

[1] M. I. Dyakonov and V. I. Perel, Current-induced spin orientation of electrons in semiconductors, Phys. Lett. A **35**, 459 (1971).

[2] J. E. Hirsch, Spin Hall Effect, Phys. Rev. Lett. **83**, 1834 (1999).

[3] J. Sinova, S. O. Valenzuela, J. Wunderlich, C. H. Back, and T. Jungwirth, Spin Hall effects, Rev. Mod. Phys. **87**, 1213 (2015).

[4] L. Liu, C.-F. Pai, Y. Li, H. W. Tseng, D. C. Ralph, and R. A. Buhrman, Spin-torque switching with the giant spin Hall effect of tantalum, Science **336**, 555 (2012).

[5] S. Emori, U. Bauer, S.-M. Ahn, E. Martinez, and G. S. D. Beach, Current-driven dynamics of chiral ferromagnetic domain walls, Nat. Mater. **12**, 611 (2013).

[6] K.-S. Ryu, L. Thomas, S.-H. Yang, and S. Parkin, Chiral spin torque at magnetic domain walls, Nat. Nanotechnol. **8**, 527 (2013).

[7] G. Yu, P. Upadhyaya, Y. Fan, J. G. Alzate, W. Jiang, K. L. Wong, S. Takei, S. A. Bender, L.-T. Chang, Y. Jiang, M. Lang, J. Tang, Y. Wang, Y. Tserkovnyak, P. K. Amiri, and K. L. Wang, Switching of perpendicular magnetization by spin-orbit torques

in the absence of external magnetic fields, Nat. Nanotechnol. **9**, 548 (2014).

[8] A. Azevedo, L. H. Vilela Leão, R. L. Rodriguez-Suarez, A. B. Oliveira, and S. M. Rezende, DC effect in ferromagnetic resonance: Evidence of the spin-pumping effect? J. Appl. Phys. **97**, 10C715 (2005).

[9] E. Saitoh, M. Ueda, H. Miyajima, and G. Tatara, Conversion of spin current into charge current at room temperature: Inverse spin-Hall effect, Appl. Phys. Lett. **88**, 182509 (2006).

[10] Y. Niimi, Y. Kawanishi, D. H. Wei, C. Deranlot, H. X. Yang, M. Chshiev, T. Valet, A. Fert, and Y. Otani, Giant Spin Hall Effect Induced by Skew Scattering from Bismuth Impurities inside Thin Film CuBi Alloys, Phys. Rev. Lett. **109**, 156602 (2012).

[11] A. Hoffmann, Spin Hall effects in metals, IEEE Trans. Magn. **49**, 5172 (2013).

[12] M. Isasa, E. Villamor, L. E. Hueso, M. Gradhand, and F. Casanova, Temperature dependence of spin diffusion length and spin Hall angle in Au and Pt, Phys. Rev. B **91**, 024402 (2015).

[13] M. Obstbaum, M. Decker, A. K. Greitner, M. Haertinger, T. N. G. Meier, M. Kronseder, K. Chadova, S. Wimmer, D. Ködderitzsch, H. Ebert, and C. H. Back, Tuning Spin Hall Angles by Alloying, Phys. Rev. Lett. **117**, 167204 (2016).

[14] H. Wang, C. Du, P. Chris Hammel, and F. Yang, Spin current and inverse spin Hall effect in ferromagnetic metals probed by $Y_3Fe_5O_{12}$-based spin pumping, Appl. Phys. Lett. **104**, 202405 (2014).

[15] M. Kimata, H. Chen, K. Kondou, S. Sugimoto, P. K. Muduli, M. Ikhlas, Y. Omori, T. Tomita, A. H. MacDonald, S. Nakatsuji, and Y. Otani, Magnetic and magnetic inverse spin Hall effects in a non-collinear antiferromagnet, Nature **565**, 627 (2019).

[16] A. Davidson, V. P. Amin, W. S. Aljuaid, P. M. Haney, and X. Fan, Perspectives of electrically generated spin currents in ferromagnetic materials, Phys. Lett. A **384**, 126228 (2020).

[17] J. Holanda, H. Saglam, V. Karakas, Z. Zang, Y. Li, R. Divan, Y. Liu, O. Ozatay, V. Novosad, J. E. Pearson, and A. Hoffmann, Magnetic Damping Modulation in $IrMn_3/Ni_{80}Fe_{20}$ via the Magnetic Spin Hall Effect, Phys. Rev. Lett. **124**, 087204 (2020).

[18] A. M. Humphries, T. Wang, E. R. J. Edwards, S. R. Allen, J. M. Shaw, H. T. Nembach, J. Q. Xiao, T. J. Silva, and X. Fan, Observation of spin-orbit effects with spin rotation symmetry, Nat. Commun. **8**, 911 (2017).

[19] S. C. Baek, V. P. Amin, Y.-W. Oh, G. Go, S.-J. Lee, G.-H. Lee, K.-J. Kim, M. D. Stiles, B.-G. Park, and K.-J. Lee, Spin currents and spin-orbit torques in ferromagnetic trilayers, Nat. Mater. **17**, 509 (2018).

[20] V. P. Amin, J. Zemen, and M. D. Stiles, Interface-Generated Spin Currents, Phys. Rev. Lett. **121**, 136805 (2018).

[21] T. Wang, S. Lendinez, M. B. Jungfleisch, J. Kolodzey, J. Q. Xiao, and X. Fan, Detection of spin-orbit torque with spin rotation symmetry, Appl. Phys. Lett. **116**, 012404 (2020).

[22] W. S. Aljuaid, S. R. Allen, A. Davidson, and X. Fan, Free-layer-thickness-dependence of the spin galvanic effect with spin rotation symmetry, Appl. Phys. Lett. **113**, 122401 (2018).

[23] T. C. Chuang, D. Qu, S. Y. Huang, and S. F. Lee, Magnetization-dependent spin Hall effect in a perpendicular magnetized film, Phys. Rev. Research **2**, 032053(R) (2020).

[24] Y. Hibino, T. Moriyama, K. Hasegawa, T. Koyama, T. Ono, and D. Chiba, Spin-orbit precession effect in a Py/Pt/Co tri-layer structure detected by ferromagnetic resonance, Appl. Phys. Express **13**, 083001 (2020).

[25] P. C. Kuo and C.-M. Kuo, Magnetic properties and microstructure of amorphous $Co_{100-x}Tb_x$ thin films, J. Appl. Phys. **84**, 3317 (1998).

[26] R. Q. Zhang *et al.*, Current-induced magnetization switching in a CoTb amorphous single layer, Phys. Rev. B **101**, 214418 (2020).

[27] J. Yu, D. Bang, R. Mishra, R. Ramaswamy, J. H. Oh, H.-J. Park, Y. Jeong, P. Van Thach, D.-K. Lee, G. Go, S.-W. Lee, Y. Wang, S. Shi, X. Qiu, H. Awano, K.-J. Lee, and H. Yang, Long spin coherence length and bulk-like spin-orbit torque in ferrimagnetic multilayers, Nat. Mater. **18**, 29 (2019).

[28] Y. Lim, B. Khodadadi, J.-F. Li, D. Viehland, A. Manchon, and S. Emori, Dephasing of transverse spin current in ferrimagnetic alloys, Phys. Rev. B **103**, 024443 (2021).

[29] K. Uchida, J. Xiao, H. Adachi, J. Ohe, S. Takahashi, J. Ieda, T. Ota, Y. Kajiwara, H. Umezawa, H. Kawai, G. E. W. Bauer, S. Maekawa, and E. Saitoh, Spin Seebeck insulator, Nat. Mater. **9**, 894 (2010).

[30] T. Kikkawa, K. Uchida, Y. Shiomi, Z. Qiu, D. Hou, D. Tian, H. Nakayama, X.-F. Jin, and E. Saitoh, Longitudinal Spin Seebeck Effect Free from the Proximity Nernst Effect, Phys. Rev. Lett. **110**, 067207 (2013).

[31] B. Hebler, A. Hassdenteufel, P. Reinhardt, H. Karl, and M. Albrecht, Ferrimagnetic Tb-Fe alloy thin films: Composition and thickness dependence of magnetic properties and all-optical switching, Front. Mater. **3**, 8 (2016).

[32] K. Uchida, M. Ishida, T. Kikkawa, A. Kirihara, T. Murakami, and E. Saitoh, Longitudinal spin Seebeck effect: From fundamentals to applications, J. Phys.: Condens. Matter **26**, 343202 (2014).

[33] V. P. Amin and M. D. Stiles, Spin transport at interfaces with spin-orbit coupling: Phenomenology, Phys. Rev. B **94**, 104420 (2016).

[34] V. P. Amin and M. D. Stiles, Spin transport at interfaces with spin-orbit coupling: Formalism, Phys. Rev. B **94**, 104419 (2016).

[35] M. B. Lifshits and M. I. Dyakonov, Swapping Spin Currents: Interchanging Spin and Flow Directions, Phys. Rev. Lett. **103**, 186601 (2009).

[36] H. B. M. Saidaoui and A. Manchon, Spin-Swapping Transport and Torques in Ultrathin Magnetic Bilayers, Phys. Rev. Lett. **117**, 036601 (2016).

[37] C. O. Pauyac, M. Chshiev, A. Manchon, and S. A. Nikolaev, Spin Hall and Spin Swapping Torques in Diffusive Ferromagnets, Phys. Rev. Lett. **120**, 176802 (2018).

[38] H. Kim, S. Karube, J. Borge, J. Kim, K. Kondou, and Y. Otani, Evidence for spin swapping from modulation of transverse resistance in magnetic heterostructures with Rashba interface, Appl. Phys. Lett. **116**, 122403 (2020).

[39] A. Yagmur, S. Karube, K. Uchida, K. Kondou, R. Iguchi, T. Kikkawa, Y. Otani, and E. Saitoh, Spin-current-driven thermoelectric generation based on interfacial spin-orbit coupling, Appl. Phys. Lett. **108**, 242409 (2016).

[40] D. Tian, Y. Li, D. Qu, S. Y. Huang, X. Jin, and C. L. Chien, Manipulation of pure spin current in ferromagnetic metals independent of magnetization, Phys. Rev. B **94**, 020403(R) (2016).

[41] R. Sato, N. Saito, and Y. Togami, Magnetic anisotropy of amorphous Gd-*R*-Co (*R* = Tb, Dy, Ho, Er) films, Jpn. J. Appl. Phys. **24**, L266 (1985).

[42] H. Tanaka, Y. Kato, and S. Takayama, Anisotropic atomic structure of TbFe and TbCo amorphous alloys, J. Non Cryst. Solids **150**, 21 (1992).

[43] M. Althammer *et al.*, Quantitative study of the spin Hall magnetoresistance in ferromagnetic insulator/normal metal hybrids, Phys. Rev. B **87**, 224401 (2013).

[44] A. Yagmur, S. Sumi, H. Awano, and K. Tanabe, Large Inverse Spin Hall Effect in CoTb Alloys due to Spin Seebeck Effect, Phys. Rev. Appl. **14**, 064025 (2020).

[45] A. N. Chantis, M. van Schilfgaarde, and T. Kotani, Quasiparticle self-consistent GW method applied to localized $4f$ electron systems, Phys. Rev. B **76**, 165126 (2007).

[46] T. W. Kim and R. J. Gambino, Composition dependence of the Hall effect in amorphous Tb_xCo_{1-x} thin films, J. Appl. Phys. **87**, 1869 (2000).

[47] Y. Hibino, K. Hasegawa, T. Koyama, and D. Chiba, Spin-orbit torque generated by spin-orbit precession effect in Py/Pt/Co tri-layer structure, APL Mater. **8**, 041110 (2020).